ELSEVIER

J. Non-Newtonian Fluid Mech., 72 (1997) 31–53

Journal of Non-Newtonian Fluid Mechanics

Effect of a spectrum of relaxation times on the capillary thinning of a filament of elastic liquid

V.M. Entov [a], E.J. Hinch [b,*]

[a] *Laboratory of Applied Continuum Mechanics, Institute for Problems in Mechanics RAS, pr Vernadskogo 101, 117526 Moscow, Russia*

[b] *Department of Applied Mathematics and Theoretical Physics, Cambridge University, Cambridge CB3 9EW, UK*

Received 8 October 1996; received in revised form 20 February 1997

Abstract

The capillary thinning of a filament of viscoelastic liquid, which is the basis of a microrheometer, is analyzed in terms of a multi-mode FENE fluid. After a short time of viscous adjustment, the stress becomes dominated by the elastic contribution and the strain-rate takes on a value equal to two-thirds the rate at which the stress would relax at fixed strain. This strain-rate decreases as the dominant mode changes. At late times, modes reach their finite extension limit. The fluid then behaves like a suspension of rigid rods with a large extensional viscosity, and the liquid filament breaks. Predictions are compared with the experiments of Liang and Mackley (1994). © 1997 Elsevier Science B.V.

Keywords: FENE; Viscoelastic flow; Capillary thinning; Microrheometry; Viscosity; Relaxation time

1. Introduction

While real materials often have a wide spectrum of relaxation times for the viscoelastic stress, most theoretical and numerical calculations ignore this and only use a single relaxation mode. This is not without good reason. On the theoretical side, we have only a partial understanding of how a material with relaxation time chooses to behave midway between a purely elastic and a purely viscous material. On the numerical side it is still not easy to compute with flow time-scales shorter than the relaxation time, i.e. high Deborah number, and so with a wide spectrum few of the modes can have their Deborah numbers larger than unity. Using many modes also has the danger of smearing out any interesting behaviour, and of introducing many adjustable parameters for fitting data. Finally calculations using a spectrum have normally found after much effort that the results were dominated by a single mode, the slowest.

* Corresponding author.

PII S0377-0257(97)00022-0

This paper examines a flow in which the spectrum plays a significant role. In designing a suitable problem, it is important to allow the material to select its own time-scale and not to prescribe one. Thus we must not impose a velocity and a length, as in flow past a sphere, which would set a time-scale. Instead we impose a force. We are also interested in nonlinear dynamics rather than a simple linear viscoelastic response as in simple stress relaxation. A problem which is both nonlinear and allows the material to select its own time-scale is the liquid filament rheometer (LFR), in which capillary forces squeeze a thinning liquid filament (Bazilevsky, Entov and Rozhkow [1] and Liang and Mackley [2]). After a complicated initial formation, which we do not study, the problem simplifies considerably to the stretching of a uniform circular cylinder, which is homogeneous in space and varies only in time.

Before we start, it is necessary to discuss the form of the constitutive equations. In linear viscoelasticity, a wide spectrum of relaxation times can be represented by a discrete or continuous spectrum. We choose the former, with N modes having elastic moduli g_i and relaxation times τ_i. The nonlinear development requires a non-trivial assumption: in this paper we assume that the modes are described by uncoupled FENE dumbbells with different maximum extensions L_i. This assumption is possibly appropriate to a dilute polydisperse mixture in which each species contributes independently to a separate mode. In cases in which the spectrum comes from different internal modes of a single species, one would expect considerable cross-coupling between the modes in the nonlinear regime. To our knowledge this cross-coupling has not been studied.

Given the considerable uncertainty in the constitutive equations, it is interesting to compare our predictions with observations. In some recent detailed experiments, Liang and Mackley [2] first measured the linear viscoelastic spectrum for the benchmark fluids S1 and the series A20–A100. They then tested these fluids in a LFR.

Now, for a Maxwell fluid with a single relaxation time, Bazilievsky, Entov and Rozhkow [1] have shown that in a LFR the radius decreases exponentially in time with a rate equal to one-third the stress relaxation rate. The question thus arises for a fluid with a wide spectrum which of the many relaxation times, if any, is measured by the LFR. Liang and Mackley [2] found in their experiments that the rate was approximately $\Sigma g_i/\Sigma g_i\tau_i$, except for the S1 fluid. We seek to answer the question. We also try to explain in terms of finite extensibility why the filaments break after thinning by an order of magnitude.

2. Governing equations

The LFR has been described in detail by Bazilevsky, Entov and Rozhkov [1]. Consider a uniform circular cylinder of radius $a(t)$ being squeezed by surface tension χ. Let the axial strain-rate of the axisymmetric extensional flow be $e(t)$, so that the radius decreases according to

$$\dot{a} = -\tfrac{1}{2}ea. \tag{1}$$

For the rheology, we take a FENE fluid with N uncoupled modes. We use the Chilcott–Rallison version of the FENE equations, although in the purely extensional flow differences between different versions are very minor. Each FENE mode is described by an axial deformation $A_z^i(t)$ and radial deformation $A_r^i(t)$, which in the particular stretching flow satisfy

$$\dot{A}^i_z = 2eA^i_z - \frac{f_i}{\tau_i}(A^i_z - 1), \tag{2}$$

$$\dot{A}^i_r = -eA^i_r - \frac{f_i}{\tau_i}(A^i_r - 1). \tag{3}$$

with relaxation times τ_i and FENE factors

$$f_i = \frac{L_i^2}{L_i^2 + 3 - A^i_z - 2A^i_r}, \tag{4}$$

with different finite extension limits L_i for each mode.

The boundary condition at the free surface sets the radial stress equal to the capillary pressure

$$-\frac{\chi}{a} = \sigma_{rr} = -p - \mu e + \sum_i g_i f_i A^i_r.$$

We assume that the axial stress vanished, because in the LFT the filament is attached to large stagnant drops on stationary end plates

$$0 = \sigma_{zz} = -p + 2\mu e + \sum_i g_i f_i A^i_z.$$

In these expressions for the stress, μ is the solvent viscosity and g_i are the elastic moduli of the modes. Eliminating the pressure p, we have

$$\frac{\chi}{a} = 3\mu e + \sum_i g_i f_i (A^i_z - A^i_r). \tag{5}$$

This equation gives the strain-rate e in terms of the instantaneous radius and deformations, which is then used in Eqs. (1)–(3) to evolve the radius and deformation.

For initial conditions, we take

$$a(0) = a_0,$$

and an undeformed material

$$A^i_z(0) = 1 = A^i_r(0).$$

In Section 6 we make detailed comparisons with the experiments of Liang and Mackley [2]. Before then we will illustrate our analysis with a simple 8-model with

$$\tau_{i+1} = 2^{-i}\tau_1, \qquad g_{i+1} = 2^i g_1 \quad \text{and} \quad L_{i+1} = 2^{-i/3} L_1. \tag{6}$$

This spectrum extends over two and a half decades in relaxation times. Many of the spectra of Liang and Mackley [2] have the feature that $g_i\tau_i$, i.e. the contribution to the zero-shear-rate viscosity, is approximately the same for each mode, except for a couple of very slow weak modes. The relation between the finite extension limits corresponds to polymers of the same type but different molecular weights M, for which $\tau \propto M^{3/2}$ and $L \propto M^{1/2}$. In our simple illustration, we further choose a moderately strong surface tension $\chi/a_0 \Sigma g_i = 1000/255$ and a moderately small solvent viscosity $\mu/\Sigma g_i\tau_i = 1/8$ (and sometimes 1/16 and 1/4). Again these values are not untypical.

Our analysis will depend on the surface tension being large, $\chi/a_0 \gg \Sigma g_i$. Because the total elastic modulus Σg_i is small, the elastic stress enters only when the deformation is large. Thus, at early times, studied in section 3, the stress will be dominated by the solvent viscosity contribution. Since the elastic stress is increasing rapidly when it becomes important and thus would soon exceed the driving capillary pressure, we find in section 4 that the strain-rate falls dramatically. The elastic stress then dominates. A small strain-rate is required in a second phase to stop the stress relaxing. Eventually finite extensibility has an effect, which is examined in section 5.

3. Early viscous times

The assumption of strong surface tension along with the initial conditions mean that we start with no elastic stress. Thus the initial stress is viscous, coming from the solvent viscosity. In this section we consider the early times before the elastic stress has had time to build up to a significant level. In these circumstances, Eq. (5) reduces to

$$\frac{\chi}{a} = 3\mu e.$$

Substituting this into Eq. (1) for the decrease in the radius, and integrating gives

$$a = a_0 - \frac{\chi}{6\mu}\, t. \tag{7}$$

Thus the radius of a filament of Newtonian fluid decreases linearly in time, vanishing at the viscous breakup time $t_{\mathrm{vb}} = 6\mu a_0/\chi$. For a water filament of thickness 1 mm, this is less than 1 ms.

Fig. 1 shows the decrease in the radius in time for our illustrative 8-mode model Eq. (6). The asymptotic prediction for early times Eq. (7) is given by the dotted lines. This analysis applies before the elastic stresses have had time to build up to a significant level. As after a time τ_N the fastest mode contributes a viscous stress $3g_N\tau_N e$, which is comparable to the solvent viscous stress $3\mu e$ in our illustrative example, we require that the shortest relaxation time in the spectrum be longer than the viscous breakup time $t_{\mathrm{vb}} \ll \tau_N$. In the three cases studied in Fig. 1, we have $t_{\mathrm{vb}}/\tau_N = 0.77$, 1.54 and 3.07. The agreement between the asymptotic prediction and the full numerical solution becomes less good after $t = \tau_N = 0.0039\tau_1$ for the last case.

Clearly the spectrum of relaxation times plays no role during the early viscous times, except for the fastest relaxation time possibly delimiting the end of the phase.

4. Middle elastic times

At the end of the viscous phase, the elastic stress has grown so that it is comparable with the capillary pressure and the viscous stress. The strain-rate must now drop, in order not to stretch the elastic stress beyond the capillary pressure. The viscous stress drops with the strain-rate. Thus a new balance is established between just the elastic stress and the capillary pressure. This change is dramatic in the case of strong surface tension. In the new elastic phase, the strain-rate

becomes independent of the surface tension, so long as it is large. It is also independent of the solvent viscosity.

We assume that in the elastic phase the deformation of the modes is large, $A_z^i \gg 1 > A_r^i$. This occurs if the surface tension is large, $\chi/a_0 \gg \Sigma\, g_i$, because a large elastic stress is needed, i.e. large deformations. We restrict attention in this section to deformations smaller than the finite extension limit, $A_z^i \ll L_i^2$, so that the FENE factors are $f_i = 1$. FENE effects will be studied in the next section. The deformation Eq. (2) then reduces to

$$\dot{A}_z^i = 2eA_z^i - \frac{1}{\tau_i} A_z^i.$$

This can be integrated with the Eq. (1) for the radius to give

$$A_z^i = \frac{a_0^4}{a^4(t)}\, \mathrm{e}^{-t/\tau_i}. \tag{8}$$

here we have used the initial conditions, on the assumption that the full relaxation term $(A_z^i - 1)/\tau_i$ has little effect during the short initial viscous phase.

Neglecting the viscous stress and the radial term A_r^i in the stress balance (5), we have

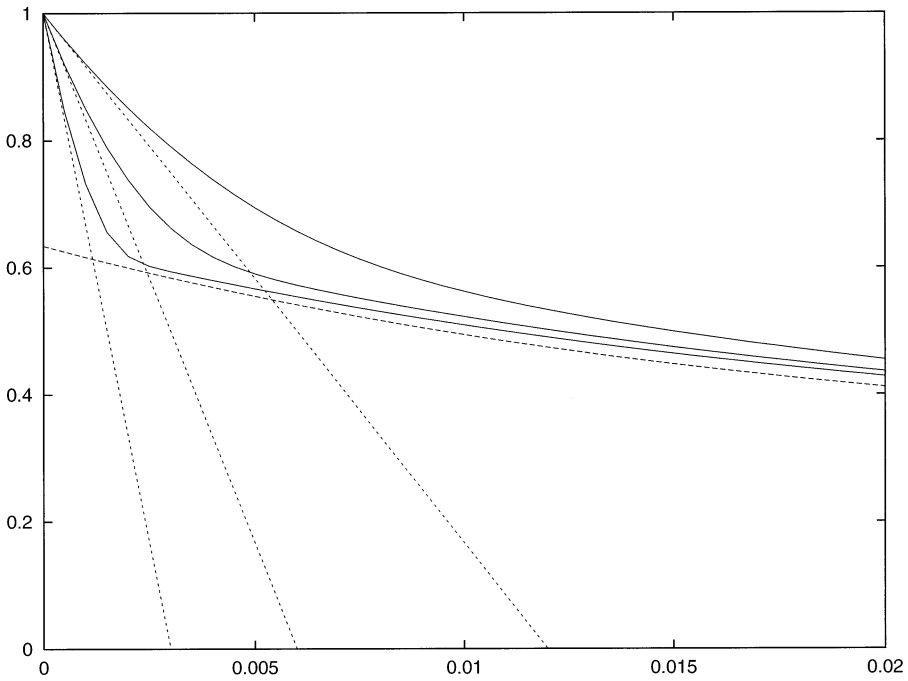

Fig. 1. Early viscous times. The decrease in the radius $a(t)/a_0$ as a function of time t/τ_1, with the 8-mode model Eq. (6), $\chi/a_0 g_1 = 10^3$ and $\mu/g_1\tau_1 = 0.5$, 1 and 2. The dotted lines are the asymptotic result Eq. (7) for early viscous times. The dashed curve is the asymptotic result Eq. (9) for the middle elastic times.

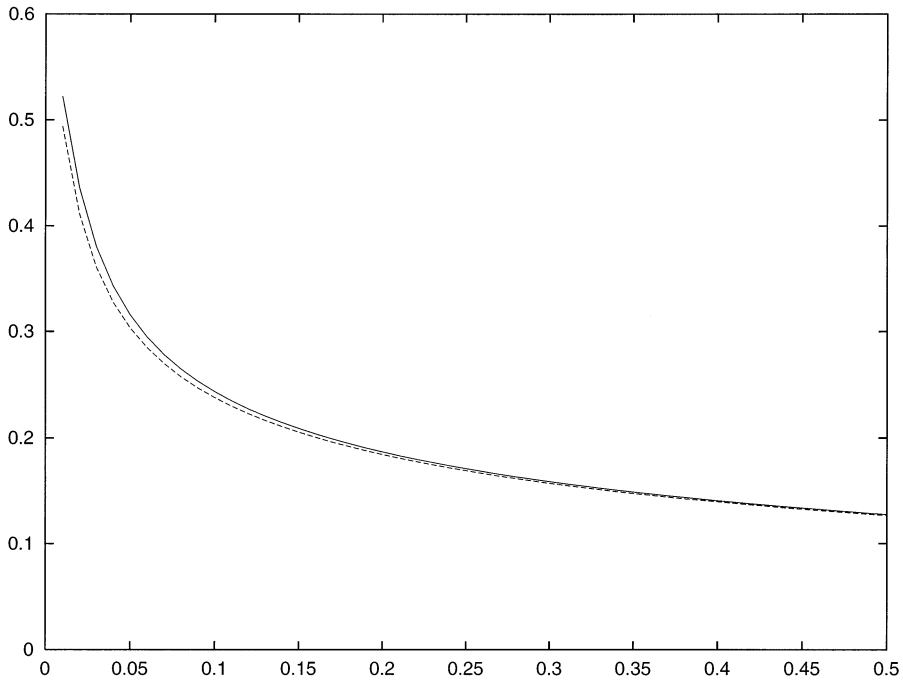

Fig. 2. Elastic phase. The decrease in the radius $a(t)/a_0$ as a function of time t/τ_1, with the 8-mode model Eq. (6), $\chi/a_0 g_1 = 10^3$ and $\mu/g_1\tau_1 = 1$. The dashed line is the asymptotic result Eq. (9).

$$\frac{x}{a} = \sum g_i A_z^i.$$

Substituting our expression Eq. (8) for A_z^i, we predict the decrease in the radius in the elastic phase

$$a(t) = a_0\left(\frac{a_0 G(t)}{\chi}\right)^{1/3}, \tag{9}$$

where

$$G(t) = \sum g_i \mathrm{e}^{-t/\tau_i}. \tag{10}$$

The function $G(t)$ is the linear stress-relaxation function for the material. If the material were subjected instantaneously to a sudden shear γ, then the shear stress would relax according to $\gamma G(t)$. Eq. (10) is for discrete spectra, with an obvious generalisation for a continuous spectra. For our particular spectrum Eq. (6) with $g_i\tau_i$ constant, an asymptotic evaluation of the sum for $\tau_N \ll t \ll \tau_1$ finds $G \sim 1.44 g_1\tau_1/t$.

Fig. 1 compares the asymptotic result Eq. (9) for the decrease in radius in time with the full numerical solution for three values of the solvent viscosity $\mu/g_1\tau_1 = 0.5$, 1 and 2. We see that, after the initial viscous phase which does depend on the value of the solvent viscosity, all three cases approach the same asymptote which does not depend on the viscosity. Fig. 2 continues the

plot to later times for the one case $\mu/g_1\tau_1 = 1$. Finite extension effects have been suppressed by setting L_1 equal to a very large number. The asymptotic prediction Eq. (9) is found to be good, despite the large surface tension parameter of $\chi/a_0 \Sigma g_i = 1000/255$ not being very large.

The quasi-exponential decrease of the radius in time Eq. (9) means that the liquid filament does not break in this elastic regime. Later, neglected finite extensibility will become important. We also observe that, if a filament starts with an initial radius varying slowly along the filament, Eq. (9) means that differences in the radius increase by only the additional factor $a_0^{1/3}$, and thus do not produce a necking instability. This stability of the filaments follows from the stress being saturated by the elastic contribution. We suggest that this mechanism may explain the stability of viscoelastic liquids in spinning.

Another test of our analysis for strong surface tension is to compare the predictions for the contributions of the modes to the stress, $g_i f_i (A_z^i - A_r^i)$. We have assumed in this section that $A_z^i \gg A_r^i$ and that $f_i = 1$, so Eq. (9) for the deformation yields contributions

$$g_i \frac{a_0^4}{a^4(t)} \mathrm{e}^{-t/\tau_i}.$$

These estimates are compared in Fig. 3 with the contributions in the full numerical solution. The agreement is good, again despite the large parameter not being particularly large.

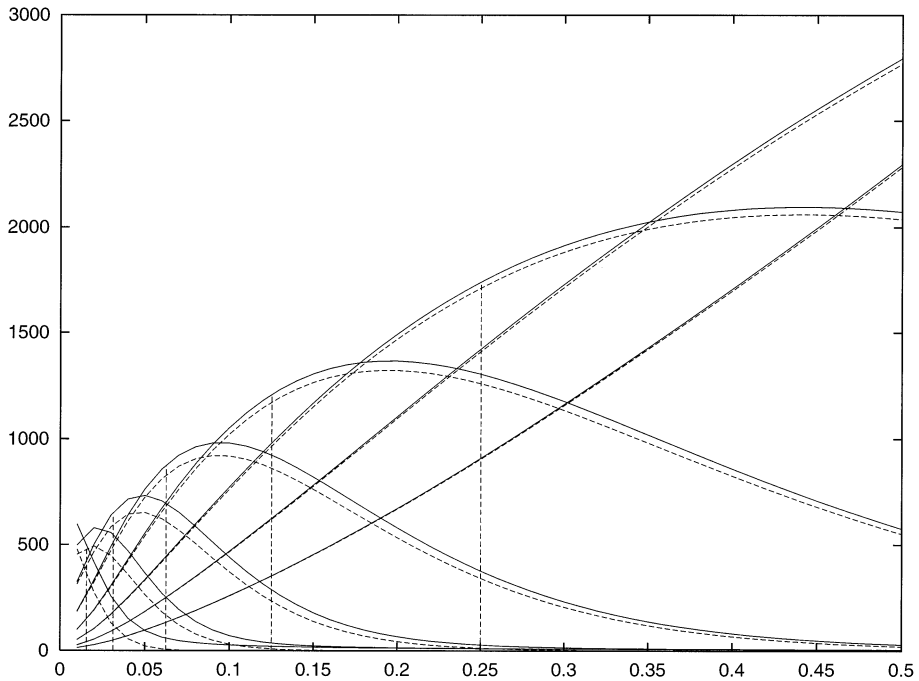

Fig. 3. Elastic phase. The contributions to the stress $g_i(A_z^i - A_r^i)/g_1$ from the 8 different modes as a function of time t/τ_1, for the model Eq. (6), $\chi/a_0 g_1 = 10^3$ and $\mu/g_1\tau_1 = 1$. The vertical lines mark where $t = \tau_i$ for the mode. The dashed lines are the asymptotic prediction $g_i a_0^4 \mathrm{e}^{-t/\tau_i}/a^4(t) g_1$.

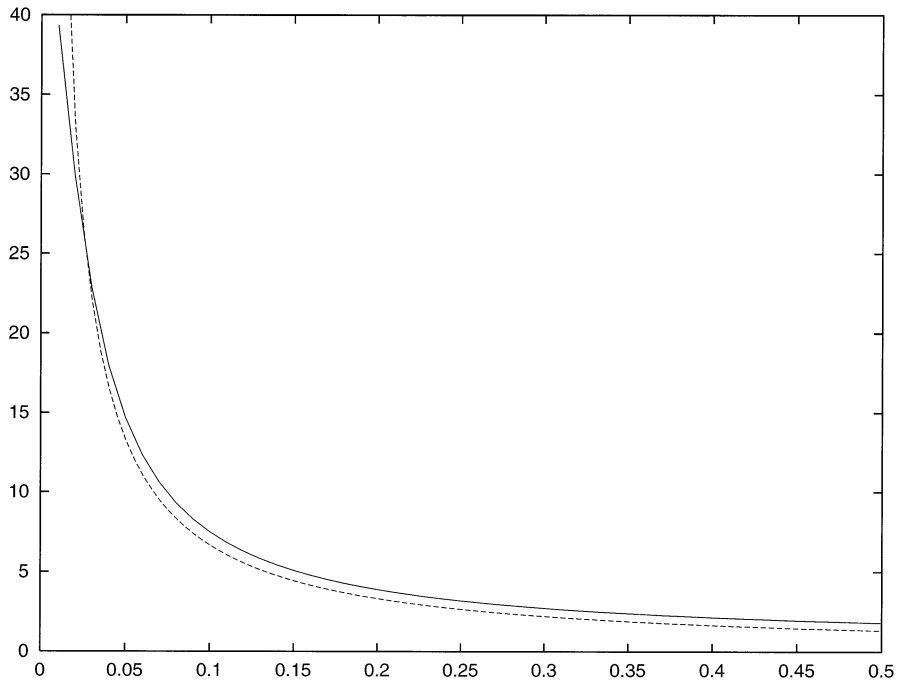

Fig. 4. Elastic phase. The strain-rate $e\tau_1$ as a function of time t/τ_1, for the model Eq. (6). $\chi/a_0 g_1 = 10^3$ and $\mu/g_1\tau_1 = 1$. The dashed curve is the approximation $e \sim 2/3t$.

Fig. 3 shows that the stress is dominated by the modes in succession: the modes with high moduli decay rapidly giving way to weaker slower-decaying modes. From the points marked on the contributions at $t = \tau_i$, we see that the mode which dominates at time t is the one with the relaxation time nearest to t. This conclusion applies to spectra similar to our illustrative example with $g_i\tau_i$ constant.

The strain-rate in the elastic phase can be found by substituting Eq. (9) with Eq. (10) for the radius decreasing in time into Eq. (1):

$$e = -\frac{2\dot{G}}{3G} = \frac{2\sum g_i \tau_i^{-1} \mathrm{e}^{-t/\tau_i}}{3\sum g_i \mathrm{e}^{-t/\tau_i}}. \tag{11}$$

Thus the strain-rate at time t is two-thirds the rate at which stress relaxes at the same time in a standard stress-relaxation experiment with fixed strain applied at the initial time. Given the conclusion from Fig. 3 that at time t the mode which dominates $G(t)$ is that with the relaxation rate τ_i nearest to t, we expect $e \sim 2/3t$ for $\tau_N < t < \tau_1$. Beyond $t = \tau_1$ when the slowest mode dominates, one would expect the strain-rate to be constant, $e \sim 1/3\tau_i$. In Fig. 4 we plot the strain-rate as a function of time. The above estimate is seen to be within a factor of 30% over the wide range of variation.

As explained at the beginning of this section, in the elastic phase the stress is elastic, equal in value to the capillary pressure. The only reason for a non-zero strain-rate is to stop the elastic stress relaxing. In an axisymmetric extensional flow, the axial strain-rate required to stop the stress relaxing is one half the stress relaxation rate, not the two thirds we have found. The additional one sixth is required because the existence of the stretching flow means that the radius decreases, and so to balance the slowly increasing capillary pressure the elastic stress must also increase slightly.

Finally, we comment that the way in which the radius decreases in the elastic phase is critically dependent on the spectrum of relaxation times, and could not be simply represented by a single mode.

5. Late times limited by finite extension

As the deformation A_z^i increases, the finite extension limit L_i eventually has an effect and we enter a new phase.

At the late times of finite extension effects, the numerical system of Eq. (5) in Eqs. (1)–(3) is very stiff. The stiffness is particularly acute for large finite extension limits or low solvent viscosities (as in the A20–A100 series of fluids). The problem is that, when the stress is dominated by the elastic part, the viscous part, which is used to calculate the strain-rate e, is the small difference of large numbers. Using the ideas of the previous section, we can develop an alternative expression for the strain-rate to use in this situation.

Once the viscous part of the stress is small, Eq. (5) becomes a balance between capillary pressure and elastic stress

$$\frac{\chi}{a} = \sum g_i f_i (A_z^i - A_r^i)$$

In this section we do not assume that the radial deformation is negligible, because the fast modes can be highly relaxed at the beginning of the phase. Also, we do not assume that the FENE factors are unity. Differentiating the equation above with respect to time, we have

$$-\frac{\chi}{a^2}\dot{a} = \sum g_i \left[\dot{A}_z^i \frac{\partial}{\partial A_z^i} f_i (A_z^i - A_r^i) + \dot{A}_r^i \frac{\partial}{\partial A_r^i} f_i (A_z^i - A_r^i) \right].$$

We now substitute Eqs. (1)–(3) for the time derivatives. This yields an expression which is linear in the strain-rate e and the relaxation rates $1/\tau_i$. Solving for e and using Eq. (4) for f_i, we find

$$e = \frac{\sum g_i f_i^3 (A_z^i - A_r^i)/\tau_i}{\sum g_i f_i [\frac{3}{2}(A_z^i + A_r^i) + 2 f_i (A_z^i - A_r^i)^2 / L_i^2]} \tag{12}$$

This approximation for the strain-rate was used in the numerical calculations once the viscous stress dropped below 1% of the total stress. The resulting numerical problem still requires caution as the finite extension limit is approached. Reducing the time-step so that the FENE factors increased by a small factor each step proved adequate.

Eq. (12) for the strain-rate is the generalisation of the earlier two-thirds the stress-relaxation rate. It is based on the same physical balance, being the strain-rate necessary to stop the FENE elastic stress relaxing from the value which balances the slowly increasing capillary pressure.

Fig. 5 gives the decrease of the radius in time with the finite extension limit $L_1 = 50$ (and so $L_8 = 7.9$). Compared with the result (9) in Section 4, we see that this large finite extension limit has little effect before $t = \tau_1$. On the other hand, the stress contributions given in Fig. 6 show considerable change before $t = 0.5\tau_1$. Once the FENE factors exceed 1.3, the stress contributions relax faster. Thus the slowest mode comes to dominate earlier, in our example by $t = 0.43\tau_1$ compared with $t = 0.6\tau_1$ without FENE effects. Because the faster modes have relaxed early, the dominant slower modes must bear more stress than the infinitely extensible case.

After $t = \tau_1$, the radius decreases faster than the infinitely extensible case given by Eq. (9), see Fig. 5. We see that the filament breaks after a finite time only when we take into account finite extensibility. The precise time of breakup depends on the value of the finite extension limit L_1. For $L_1 = 50$, the time of breakup is $2.2\tau_1$. We return to the dependence of the breakup time upon the finite extension limit at the end of the section.

As the time of breakup is approached, the slower modes are virtually fully extended, $A_z^i \sim L_i^2$, while the strain-rate e tends to infinity. Under these conditions, the rate of increase in the deformation $\dot{A}_z^i$ in Eq. (2) becomes negligible, as does the 1 in the relaxation term. Hence Eq. (2) reduces to

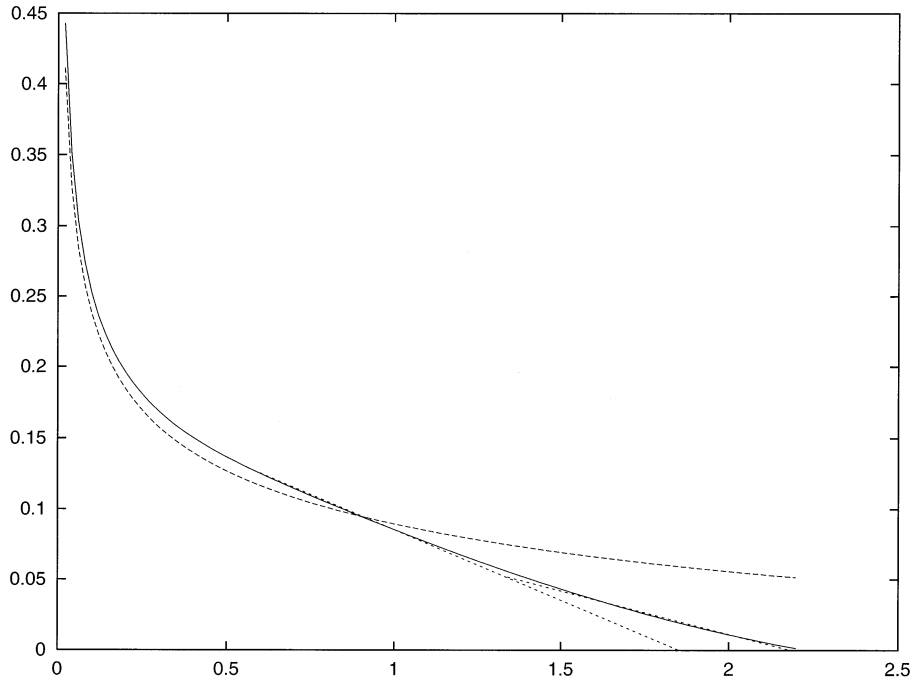

Fig. 5. FENE effects. The decrease in the radius $a(t)/a_0$ as a function of time t/τ_1, with the 8-mode model Eq. (6), $\chi/a_0 g_1 = 10^3$, $\mu/g_1\tau_1 = 1$ and $L_1 = 50$. The dashed curve is the asymptotic result Eq. (9) for infinitely extensible dumbbells. The dotted lines are the predictions Eq. (15) using an effective viscosity $\mu^* = 1667 g_1\tau_1$ (mode 1 only) for $t < 1.35\tau_1$, and $\mu^* = 2716 g_1\tau_1$ (modes 1 and 2) for $t > 1.35\tau_1$.

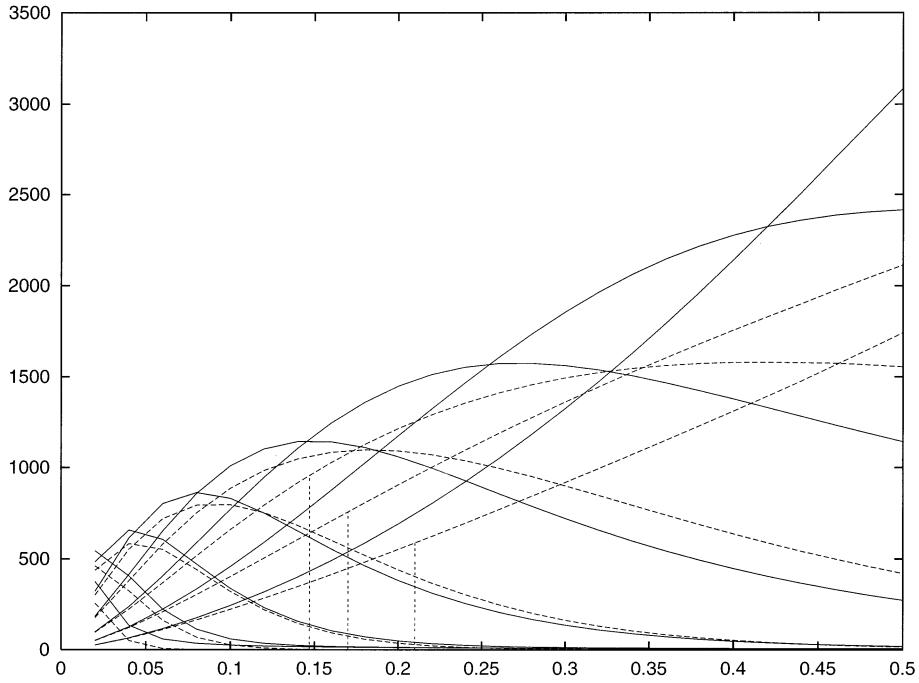

Fig. 6. FENE effects. The contributions to the stress $g_i f_i(A^i_z - A^i_r)/g_1$ from the 8 different modes as a function of time t/τ_1, for the model Eq. (6), $\chi/a_0 g_1 = 10^3$, $\mu/g_1\tau_1 = 1$ and $L_1 = 50$. The dashed lines are the asymptotic prediction $g_i a_0^4 \mathrm{e}^{-t/\tau_i}/a^4(t)g_1$ for infinitely extensible dumbbells. The vertical lines are where $f_i = 1.3$ for that mode.

$$0 \sim 2eA^i_z - \frac{f_i}{\tau_i} A^i_z.$$

Thus the FENE factors are given by

$$f_i \sim 2e\tau_i. \tag{13}$$

Hence the contribution to the stress for the modes becomes

$$2g_i\tau_i L_i^2 e.$$

To the extent that this contribution to the stress is proportional to the instantaneous strain-rate, and that the dumbbells are nearly locked rigidly at their maximum extension, we can say that the FENE fluid is now behaving like a suspension of rigid rods, with an effective viscosity

$$\mu^* = \frac{2}{3}\sum g_i\tau_i L_i^2. \tag{14}$$

The sum here is to be taken over the highly stretched modes.

As the FENE fluid in now behaving as a viscous fluid, we can apply the analysis of section 3 with the radius decreasing linearly in time at a rate inversely proportional to the effective viscosity. The approach to breakup at time $t = t_b$ is thus predicted to be

$$a = \frac{\chi}{6\mu^*}(t_b - t). \tag{15}$$

Fig. 5 shows this piecewise linear decrease, using the effective viscosity corresponding to one highly stretched state up to $t = 1.35\tau_1$ and two modes thereafter. It would perhaps be appropriate to use three modes after $t = 1.86\tau_1$, and further modes a little later, but they have little effect in the linear extrapolation to breakup. Note that the linear extrapolation with just one mode in Fig. 5 is not poor.

Associated with the linearly decreasing radius Eq. (15), section 3 predicts the strain-rate increasing rapidly towards breakup

$$e = \frac{2}{t_b - t}.$$

Combining this with the earlier expression Eq. (13) for the FENE factors, we find the growth of the deformations of the modes towards breakup

$$A_z^i = L_i^2\left(1 - \frac{t_b - t}{4\tau_i}\right). \tag{16}$$

This prediction of a linear approach to full extension at time of breakup is compared in Fig. 7 with the full numerical solution.

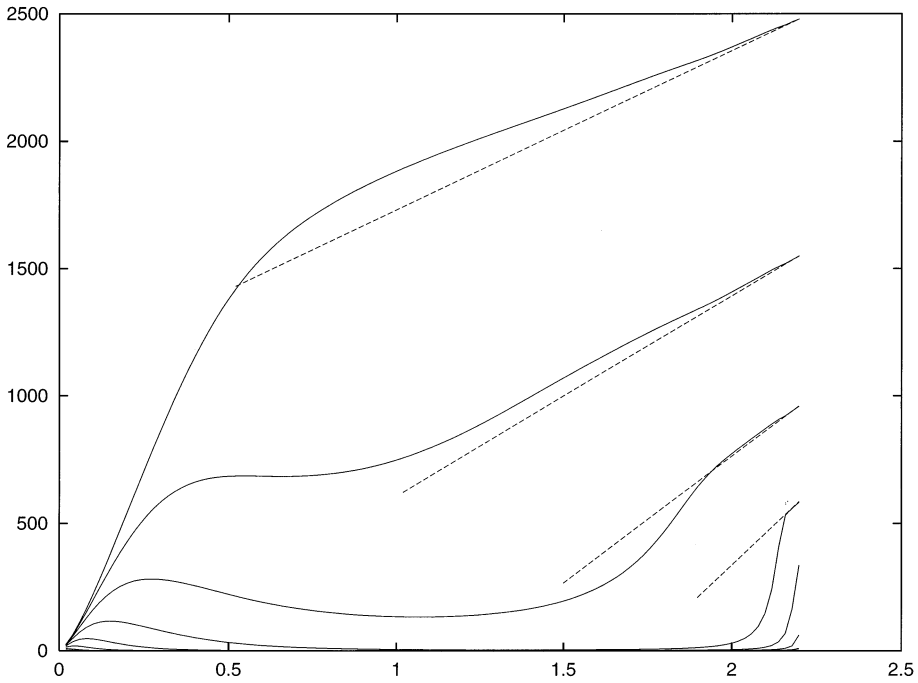

Fig. 7. FENE effects. The deformations A_z^i of the modes as functions of time t/τ_1, for the model Eq. (6), $\chi/a_0 g_1 = 10^3$, $\mu/g_1\tau_1 = 1$ and $L_1 = 50$. The dashed lines are the asymptotic prediction Eq. (16).

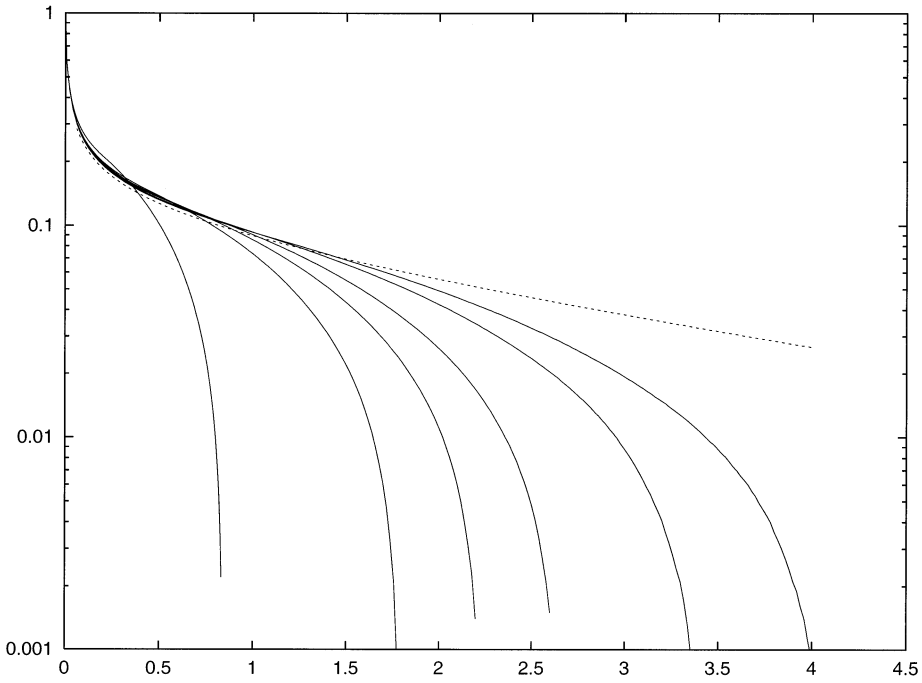

Fig. 8. FENE effects. The decrease in radius $a(t)/a_0$ as a function of time t/τ_1 for different finite extension limits from left to right $L_1 = 20$, 30, 40, 50, 60, 80 and 100, for the model Eq. (6), $\chi/a_0 g_1 = 10^3$ and $\mu/g_1\tau_1 = 1$. The dashed curve is the asymptotic result Eq. (9) for infinitely extensible dumbbells.

The dependence of the breakup time on the finite extension limit is studied in Figs. 8 and 9. Fig. 8 gives the decrease in time of the radius of the filament for various values of the finite extension limit L_1. Note that the longer dumbbells need to be stretched for a longer time before they begin to deviate from the infinitely extensible result Eq. (9). The times for breakup are plotted in Fig. 9 as a function of the finite extension limit.

The time to breakup can be estimated by patching together our two asymptotic approximations Eqs. (9) and (15), the first from the middle elastic times in which all the FENE factors are set equal to unity, and the second from the late times in which all the FENE factors are very large. We choose to patch these approximations for the radius of the filament at a cross-over time t_c, defined to be where their slopes are equal. Of course, at this cross-over time, the FENE factors are neither close to unity nor very large, and so neither asymptotic expression is strictly applicable. Our cross-over time is therefore but a crude estimate. Setting equal the two expressions for the time derivatives of the radius of the filament, we find t_c from

$$a_0 \frac{\dot{G}(t_c)}{3G(t_c)} \left(\frac{a_0 G(t_c)}{\chi} \right)^{1/3} = -\frac{\chi}{4 \sum g_i \tau_i L_i^2}. \tag{17}$$

The sum for the effective viscosity is taken over all modes which relax slower than the cross-over time, $\tau_i > t_c$. The breakup time then follows by the linear extrapolation Eq. (15),

$$t_b \approx t_c - \frac{3G(t_c)}{\dot{G}(t_c)}. \tag{18}$$

This estimate is compared with the full numerical solution in Fig. 9. The step in the estimate between $L_1 = 40$ and $L_1 = 50$ reflects a switch from 2 modes to 1 contributing to the sum for the effective viscosity.

For short FENE dumbbells, $L_1 \ll (\chi/a_0 g_1)^{2/3}$, the cross-over occurs in the middle of the spectrum of relaxation times. Here we may use the approximation $G(t) \sim 1.44 g_1 \tau_1 / t$ (for our particular test spectrum, Eq. (6)), which leads to $t_b = 4t_c$ and

$$t_b \approx 5.44 \tau_1 \frac{a_0 g_1}{\chi} \left(\sum_{\tau_i > t_b/4} \frac{g_i \tau_i L_i^2}{g_1 \tau_1} \right)^{3/4}.$$

This estimate is good for $L_1 \leq 40$ in Fig. 9. For long FENE dumbbells, $L_1 \gg (\chi/a_0 g_1)^{2/3}$, the cross-over occurs where the lowest mode dominates, $G(t) \sim g_1 e^{-t/\tau_1}$, which leads to $t_b = t_c + 3\tau_1$ and

$$t_b \sim \tau_1 \left(3 \ln \frac{4}{3} L_1^2 - 4 \ln \frac{\chi}{a_0 g_1} + 3 \right).$$

This expression produces the same estimates for Fig. 9 when $L_1 \geq 150$, although these estimates are about $2\tau_1$ too large. Such an error is to be expected given the crudeness of patching the asymptotic approximations, and is probably due to the finite extensibility making the radius

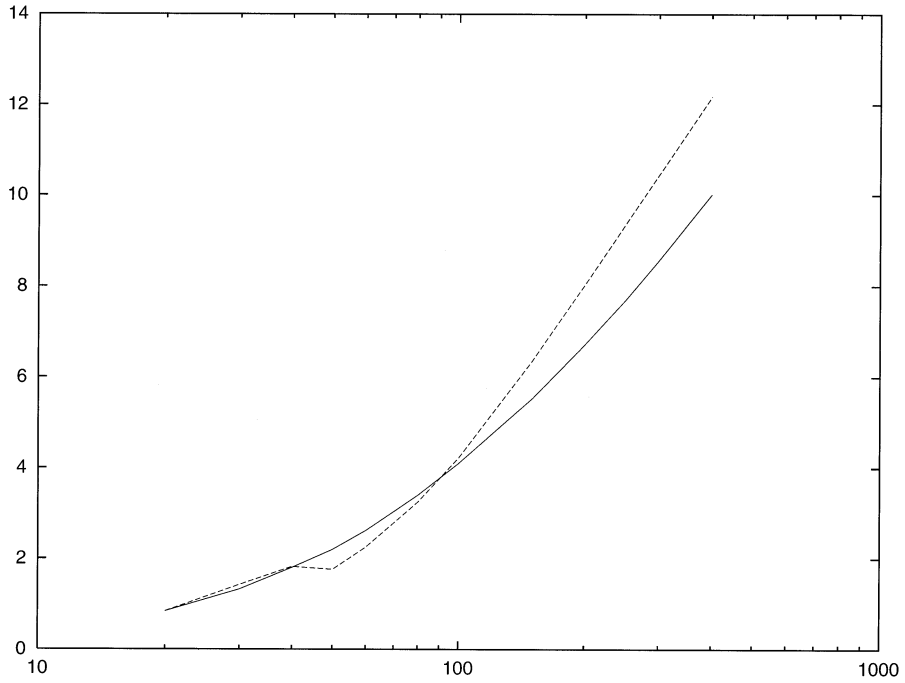

Fig. 9. FENE effects. The breakup time t_b/τ_1 as a function of the finite extension limit L_1, for the model Eq. (6), $\chi/a_0 g_1 = 10^3$ and $\mu/g_1\tau_1 = 1$. The dashed curve gives the estimate Eq. (18) with Eq. (17).

decrease more rapidly than Eq. (9) at the cross-over time. An alternative to patching the radius of the filament would be to patch the stretches Eqs. (8) and (16). This alternative suffers the difficulty of having to decide whether an intermediate mode will relax on being affected by finite extension or whether it will dominate the weaker slower modes in the stress.

There are two ways to view how finite extensibility leads to the breakup of the filament. In the elastic phase of Section 4, the strain-rate is two-thirds the current relaxation rate. An effect of finite extensibility has been seen in Fig. 6 to be to increase the relaxation rates by strengthening the springs of the dumbbells. The relaxation rates thus increase without limit, leading to a faster than exponential decrease in the radius of the filament. Alternatively, at large deformations the elastic stress of the dumbbells becomes proportional to the strain-rate, i.e. the stress appears to be viscous. We have seen in Section 3 that a viscous response produces a strain-rate proportional to $1/a$, and so the radius decreases linearly in time.

The spectrum of relaxation times does not play a central role when finite extension effects act, although they do influence when those effects come into play. A fluid with a spectrum could be adequately represented by a single mode with $g\tau L^2$ set equal to $\Sigma\, g_i\tau_i L_i^2$. With many spectra, a single mode does in fact dominate this sum over the modes.

6. Comparison with experiments

Our theoretical calculations above are based on an assumed form of the constitutive equations, a system of uncoupled FENE dumbbells. There can be no certainty that this form applies to any real material. It is therefore interesting to compare our predictions with experiments.

Recently Liang and Mackley [2] have investigated the benchmark fluids S1 and the series A20–A100. These are solutions of a commercial grade of polyisobutylene, with a wide range of molecular weights which will produce a wide spectrum of relaxation times. The S1 fluid is a 2.5% solution in 47.5% decaline and 50% polybutene oil, and the A20–A100 fluids are 1–5% solutions in decaline. Liang and Mackley measured the storage and loss moduli $G'(\omega)$ and $G''(\omega)$ in oscillating shear in the linear regime. Software in the rheometer then fitted a discrete spectrum g_i, τ_i with 11 modes spread evenly over 3 decades on a logarithmic scale, see Table 1. Nonlinear step-strain experiments were then conducted and interpreted in terms of a Wagner exponential damping function in an integral constitutive equation. This gave good predictions for the measured stress growth and measured steady viscometric functions. All these tests were made in simple shear flow.

Now we have used a FENE constitutive equation rather than an integral equation with a Wagner damping function, and it is not possible to interpret the damping coefficient k as a finite extension limit L. The damping function produces strain thinning, whereas the FENE spring produces strain hardening. The FENE modification of the linear Hookean dumbbells was introduced to control extensional flow effects, and is not good for describing nonlinear shear effects. As noted above, the good fit of the Wagner constitutive equation was only tested in simple shear. Hence, we must discard the experimental data for the damping coefficient and treat our finite extension limit L as an unknown adjustable parameter. We do however keep in full the measured linear spectrum.

Table 1
The moduli g_i (in Pa) for the different relaxation times τ_i (in seconds) for the benchmark fluids

τ_i	S1	A20	A40	A60	A80	A100
0.010	1.31e2	6.89e−1	9.97	5.29e1	1.28e2	2.65e2
0.020	3.29e−3	1.163	6.34	1.69e1	5.12e−3	1.40e−2
0.040	2.18	6.88e−1	3.09	7.23	1.80e1	4.63e1
0.079	1.47e1	1.62e−1	1.14	5.82	2.11e1	5.44e1
0.158	1.11e1	2.68e−2	3.05e−1	3.33	1.04e1	2.88e1
0.316	5.57	3.12e−3	6.16e−2	1.35	5.46	1.86e1
0.631	3.04	6.85e−5	9.78e−3	4.82e−1	2.84	1.15e1
1.259	1.74	1.08e−7	1.03e−3	1.22e−1	1.10	4.42
2.512	6.58e−1	2.43e−4	5.85e−9	9.13e−3	3.12e−1	1.61
5.012	7.11e−2	4.33e−4	1.55e−5	6.86e−7	6.35e−2	7.73e−1
10.00	1.73e−2	4.66e−4	9.64e−5	7.57e−3	2.73e−2	9.11e−2

For our comparisons, we also need values for the surface tension and the solvent viscosity. We take $\chi = 3 \times 10^{-2}$ N m^{-1} and $\mu = 3$ Pa s for S1 and $\mu = 2.41 \times 10^{-3}$ Pa s for A20–A100. The asymptotic theory tells us that the results are reasonably insensitive to the values selected for these parameters.

After characterising the rheology of the benchmark fluids, Liang and Mackley then placed a sample of the fluids in the Liquid Filament Rheometer. They measured the capillary thinning of a liquid filament (see their Fig. 13). The initial diameters of the filaments were 2.44 mm (S1), 0.45 mm (A20) and 0.9 mm (A40–A100). The diameters decreased to 0.02 mm over a time of 16–0.3 s depending on the fluid.

The experimental results show no early viscous phase. With the parameters of the experiments, this phase is expected either to be very short ($t_{vb} = 2.2 \times 10^{-4}$ s or less) for the A20–A100 fluids, or to be unnecessary because of low surface tension ($\chi/a_0 \Sigma g_i = 0.15$ for S1 and A100, and 0.36 for A80). In the former case, the phase will occur in times shorter than those resolved by the experiments, and most probably during the setting up of the initial filament. This is a problem with the Liquid Filament Rheometer, that the process of making the initial filament is not yet well characterised. Thus we do not know how much the material is deformed during the process. For the fluids S1, A80 and A100 we choose to assume that the material is not deformed, i.e. the initial conditions $A_z^i(0) = 1 = A_r^i(0)$ are satisfied. For the other fluids it is necessary to assume that the material is deformed before measurements start. For these cases we assume a pre-stretch P, setting

$$A_z^i(0) = P\,\frac{L_i^2}{L_i^2 + P} \quad \text{and} \quad A_r^i(0) = \frac{1}{P^{1/2}}\,.$$

This corresponds to the length of the filament being stretched by a factor of P^2 by the combination of the setting up and the rapid viscous phase. The arbitrary factor $L_i^2/(L_i^2 + P)$ is necessary to stop modes being stretched beyond their finite extension limit. The value of the pre-stretch was adjusted so that the radius changed least at the beginning of the numerical calculations. One would anticipate this value to be $P = a_0 \Sigma g_i/\chi$, in order that the elastic stresses start in balance with the capillary pressure.

First we consider the S1 fluid. This fluid has a solvent viscosity which is not small, but which is 21% of the total solution viscosity (at zero shear-rate). Also, as noted above, the capillary pressure is not large compared with the total elastic modulus, $\chi/a_0 \Sigma g_i = 0.15$, although after the fastest mode relaxes at 0.01 s the ratio increases to 0.63, and after the further 0.3 s it increases to 2.2. Thus the capillary thinning of the S1 fluid is not entirely within the asymptotic analysis of Section 4. Numerical solution can however be made of the governing equations.

Fig. 10 gives the decrease in diameter as a function of time. The points are the experimental observations of Liang and Mackley. The three continuous curves are the numerical solutions using the experimental spectrum with three choices of the finite extension limit, $L_1 = 17$, 20 and 22. No pre-stretch was applied. The best fit of the adjustable parameter is $L_1 = 20$. We note that Eqs. (17) and (18) predict $L_1 = 47$ using the observed breakup time of 16 s. Also plotted in Fig. 10 is the prediction Eq. (9) for the middle elastic times. This has the correct magnitude until the finite extension limit is felt. Discrepancies at early times may be due to the fastest modes ($\tau_i = O(0.01\,\text{s})$) having relaxed before the first experimental observation. Also, the viscous breakup time t_{vb} is 0.73 s, due to the large solvent viscosity, and this is not small compared with the fastest relaxation times.

Fig. 11 shows the deformation of the various modes for $L_1 = 20$. Note the linear approach to the maximum extension, as predicted by Eq. (16). Fig. 12 shows for the contributions of the different modes to the stress for $L_1 = 20$. Note that the slowest mode never dominates, because its modulus is so low. It is the second slowest mode which dominates for most of the time.

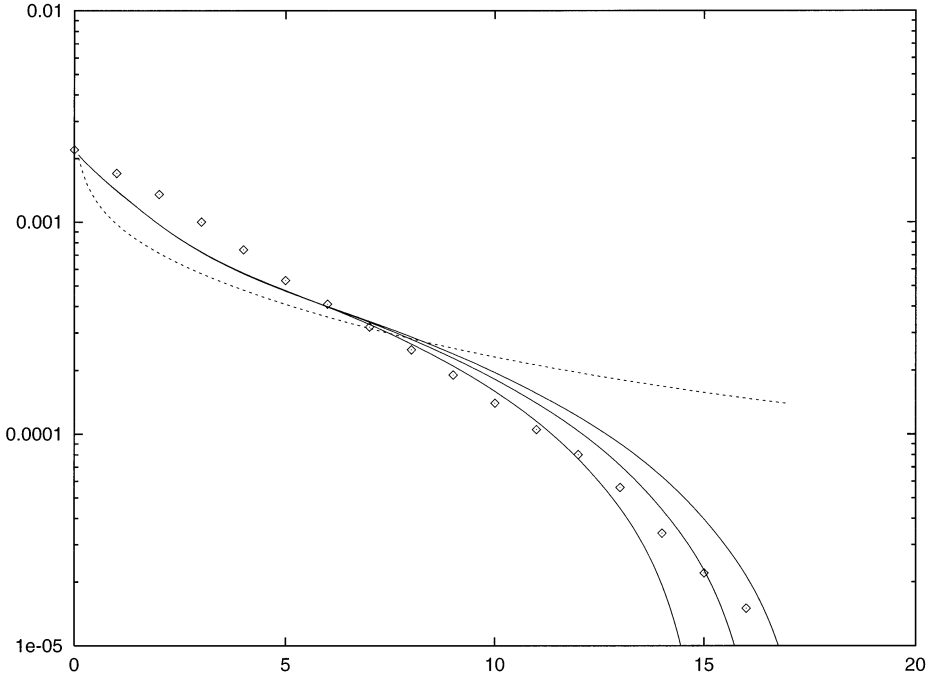

Fig. 10. S1 fluid. The decrease in the diameter $2a(t)$ (in m) as a function of time (in s). The diamonds are the experimental observations of Liang and Mackley. The three continuous curves are, from the left, predictions for $L_1 = 17$, 20 and 22. The dashed curve is the asymptotic result $2a_0(a_0 G(t)/\chi)^{1/3}$.

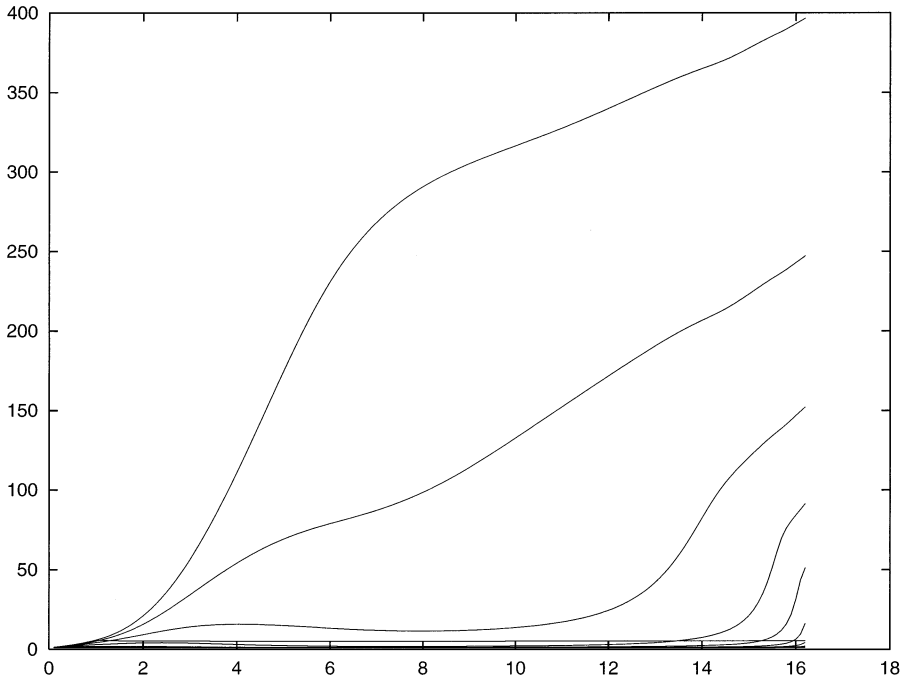

Fig. 11. S1 fluid. The increase in the deformations $A_z^i(t)$ as a function of time (in s) for the case $L_1 = 20$.

Fig. 13 shows the decrease in diameter for the fluid A20. This fluid has strong surface tension, $\chi/a_0 \Sigma g_i = 45$, and so one would expect a rapid viscous phase to produce a pre-stretch of about this value. In fact the experimental data are best fitted (with no jump near $t = 0$) with just this pre-stretch $P = 45$. With this optimal value of the pre-stretch, the full numerical solution and a modified asymptotic result for middle elastic times, $a_0(Pa_0G(t)/\chi)^{1/3}$, which takes into account the pre-stretch, both follow the experimental data fairly well until the finite extension limit is felt. The breakup time of $t = 0.3$ s is best fitted with a finite extension limit $L_1 = 77$. The approximate theory of Eq. (18) with Eq. (17), modified to incorporate the pre-stretch, gives the poor estimate $L_1 = 38$.

Fig. 14 shows the decrease in diameter for the fluids A40–A100. For A40, the initial capillary pressure χ/a_0 is 3.19 times the total elastic modulus Σg_i, but this doubles after the fastest mode relaxes at $t = 0.01$ s, and doubles again when the next mode decays at $t = 0.02$ s. A pre-stretch of 5 was found necessary to avoid an early jump in the diameter. The best fit of the breakup at $t = 0.7$ s was obtained with a finite extension limit of $L_1 = 77$. The approximate theory of Eq. (18) with Eq. (17) modified to incorporate the pre-stretch gives the estimate $L_1 = 89$. For A60, with an initial capillary pressure of 0.76 times the total elastic modulus, a pre-stretch of 3 and a finite extension of $L_1 = 24$ (cf. 15 from Eq. (18) with Eq. (17)) fitted the experimental data. For A80 and A100, with initial capillary pressures of 0.36 and 0.15 times the total elastic modulus, the experimental data was best fitted with $L_1 = 4.5$ and 0.84 (cf. 6.5 and 3.2 from Eq. (18) with Eq. (17)). These values for L_1 are of course absurd if one interprets them as the finite extension limit of a polymer molecule. The results for the fitting parameters are summarised in Table 2.

Using the two adjustable parameters, the pre-stretch P which is adjusted to avoid an initial jump in the diameter and the finite extension limit L_1 which is adjusted to fit the breakup time, the experimental observations of Liang and Mackley of the capillary thinning have been fitted reasonably well using their measured spectra with the wide range of relaxation times. There are some discrepancies at early times, which are probably due to the fastest modes having relaxed before the first observation. The poor characterisation of the initial filament is a problem with the Liquid Filament Rheometer which needs to be addressed in the future.

Our asymptotic theory Eq. (9) for the middle elastic times also predicts the experiments reasonably well until the finite extension limit is felt, despite in most cases the initial capillary pressure not being much greater than the total elastic modulus. It would be possible to develop an alternative theory for weak capillary pressure, but this would in effect be linear viscoelasticity producing the viscous estimates of Section 3 with a time-dependent viscosity $\mu^*(t) = \mu + \Sigma\, g_i\tau_i$, where the sum is taken over the modes which have had time to relax, $\tau_i < t$. In the LFR experiments however, as soon as a few of the fastest modes (with the highest moduli) have decayed, the capillary pressure does become larger than a sum over the remaining moduli, and so our theory Eq. (9) becomes applicable.

The predictions for the finite extension limit by the approximate theory Eq. (18) with Eq. (17) are not good compared with the full numerical solutions, particularly for the cases involving a pre-stretch.

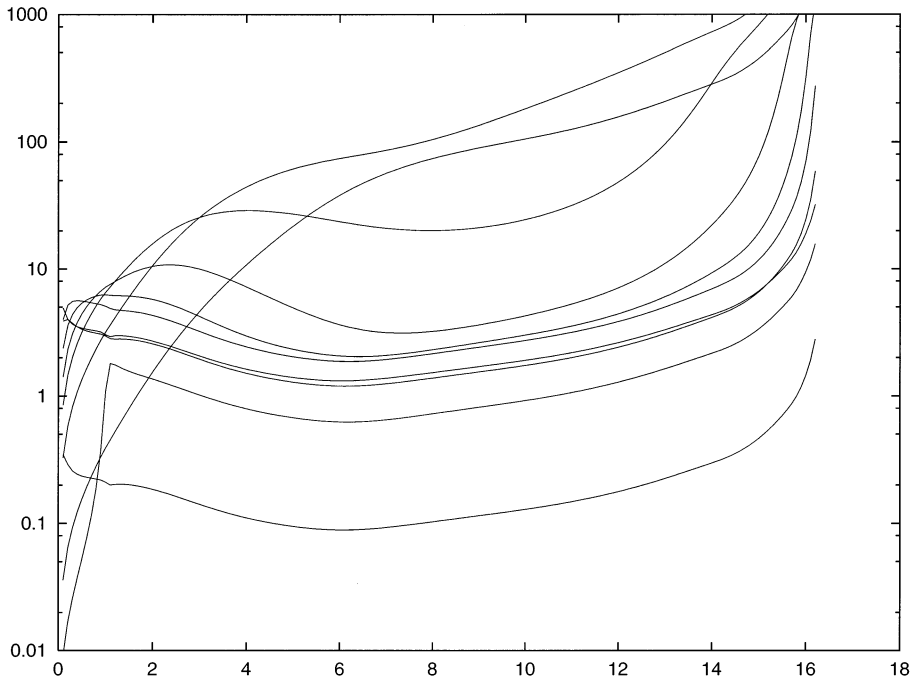

Fig. 12. S1 fluid. The stress contributions $g_i f_i(A_z^i - a_r^i)$ (in Pa) as a function of time (in s) for the case $L_1 = 20$. At $t = 10$ s the modes are, from the top, $i = 2$, 1, 3, 4, 5, 6, 10, 7, 11, 8, 9, where $\tau_1 = 10$ s and $\tau_{11} = 0.01$ s.

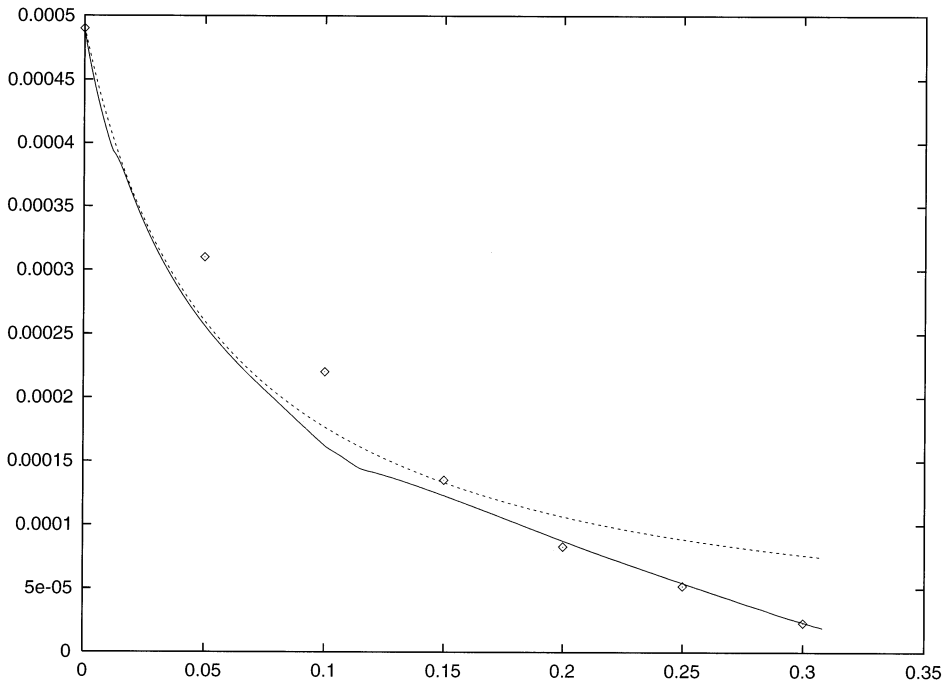

Fig. 13. A20. The decrease in the diameter $2a(t)$ (in m) as a function of time (in seconds). The diamonds are the experimental observations of Liang and Mackley. The continuous curve is for $L_1 = 77$ and a pre-stretch $P = 45$. The dashed curve is the asymptotic result $2a_0(Pa_0G(t)/\chi)^{1/3}$.

We can now return to the question at the end of the introduction, of what relaxation time is measured by the LFR for a fluid with a wide spectrum of relaxation times. It is instructive to compare the two fluids S1 and A80. These have virtually the same spectrum, see Table 1 and also Fig. 5 in Liang and Mackley for the storage and loss moduli $G'(\omega)$ and $G''(\omega)$. The fluids differ substantially in their solvent viscosities, by a factor of 10^3, but the solvent contributes only 20% to the solution viscosity in the larger case. Liang and Mackley further show in their Fig. 9 that the steady shear viscosity $\mu(\dot{\gamma})$ is the same for the two fluids. In the LFR, however, the capillary thinning is very different, S1 breaking after 16 s while A80 breaks after 1.8 s. Thus the simple shear flow characterisations fail to catch all of the rheology.

The experimental observations for each of the six fluids can be divided into two roughly equal periods. The first half follows, more or less, the asymptotic result Eq. (9) for the middle elastic times, the dashed curves in Figs. 10, 13 and 14. This asymptotic result does not depend on the solvent viscosity, so long as it makes a small contribution to the total viscosity, $\mu \ll \Sigma\, g_i\tau_i$. The result does depend strongly on the spectrum. As the spectra of S1 and A80 are virtually the same, the dashed curves in Figs. 10 and 14(c) are the same. Hence, the difference between the two fluids is the time at which they deviate from this asymptotic curve, $t = 8$ s for S1 and $t = 0.9$ s for A80. The fluids start to deviate from the asymptotic result, and so enter the second period of the experimental observations, when the finite extension limit comes into play. This limit would seem to be quite different for the two fluids, $L_1 = 20$ for S1 and $L_1 = 4.5$ for A80.

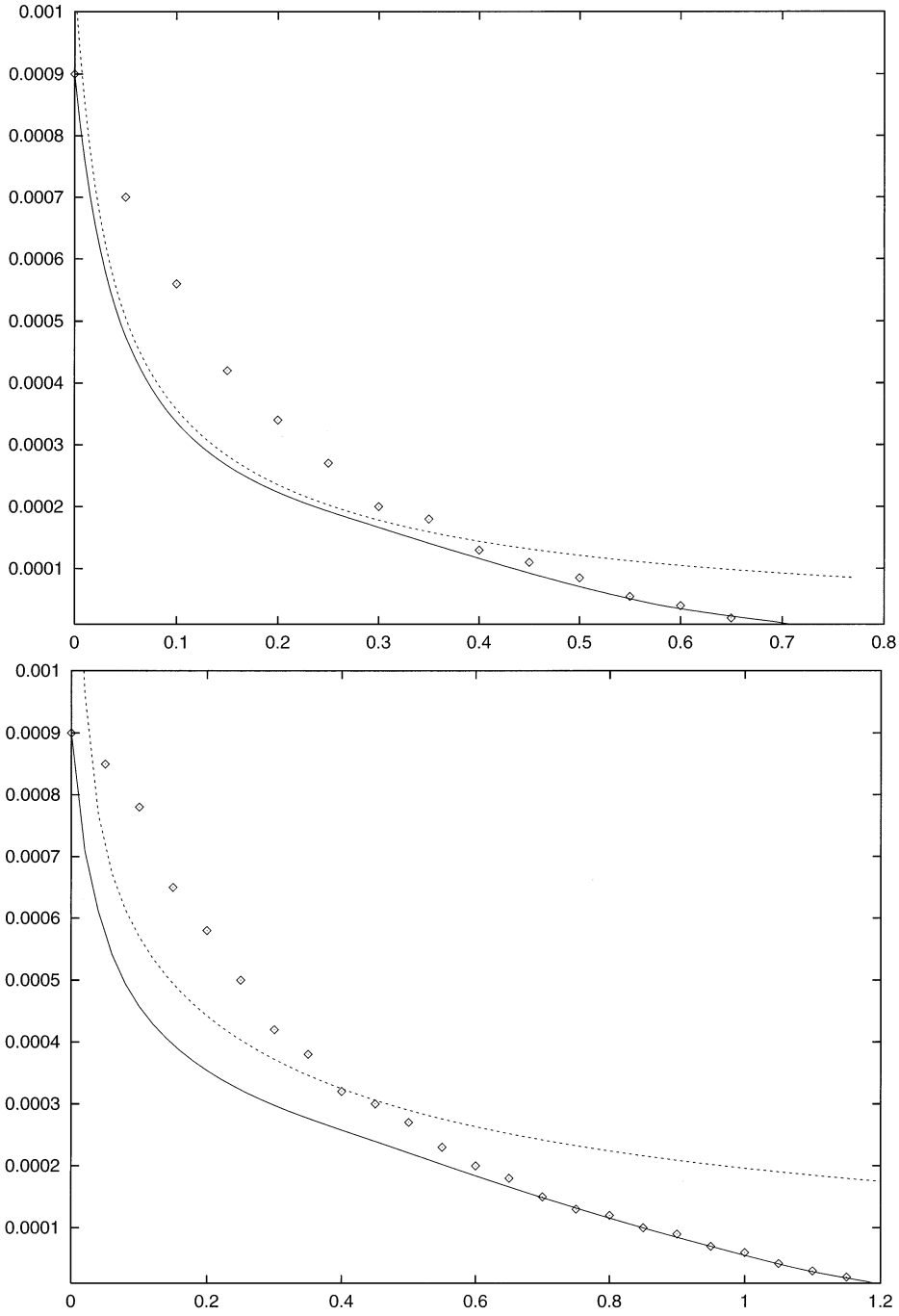
0.001
0.0009
0.0008
0.0007
0.0006
0.0005
0.0004
0.0003
0.0002
0.0001
0
0.1
0.2
0.3
0.4
0.5
0.6
0.7
0.8
0.001
0.0009
0.0008
0.0007
0.0006
0.0005
0.0004
0.0003
0.0002
0.0001
0
0.2
0.4
0.6
0.8
1
1.2

Fig. 14.

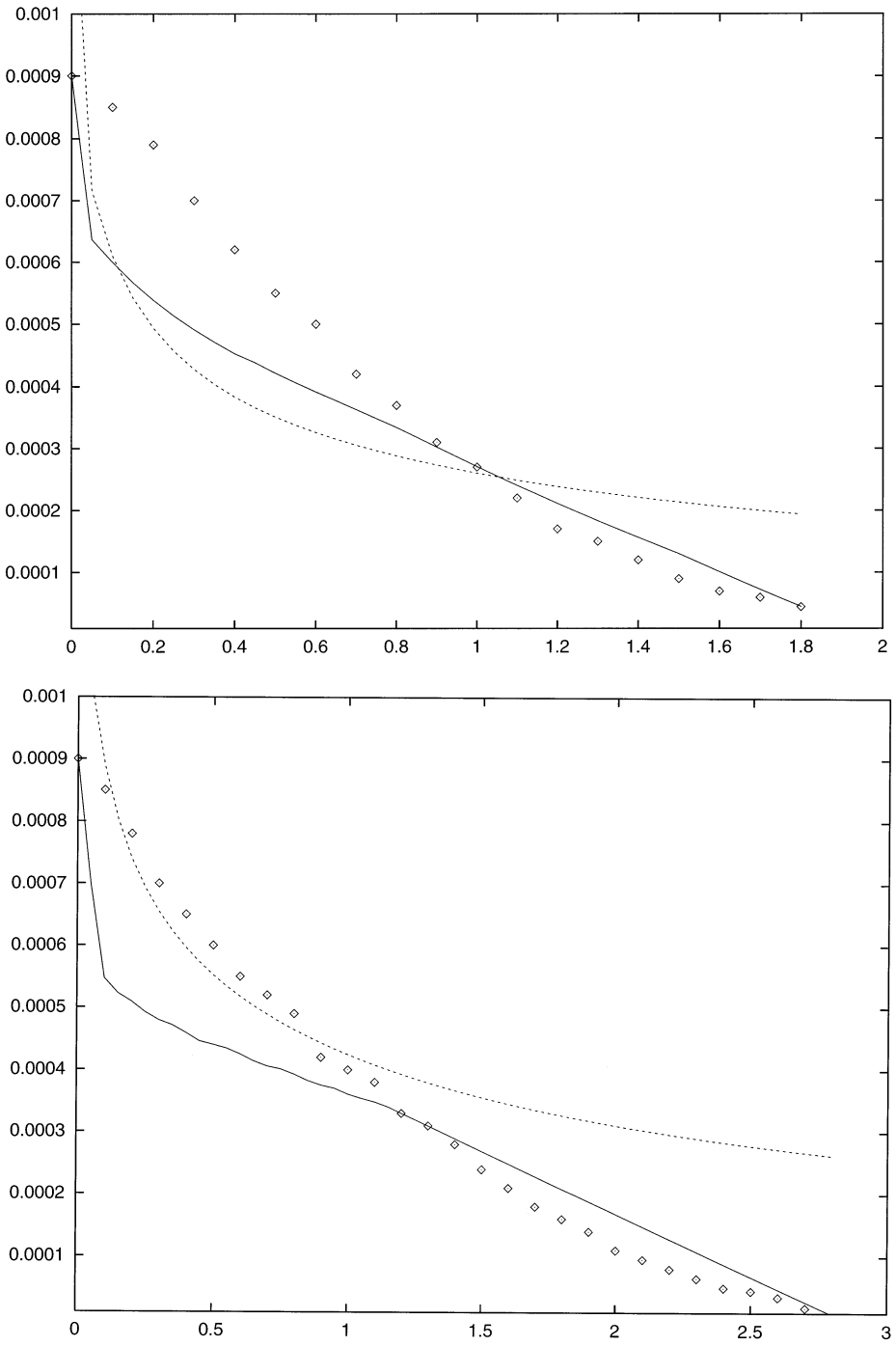

Fig. 14. A40–A100. The decrease in the diameter $2a(t)$ (in m) as a function of time (in s) for the fluids A40–A100. The diamonds are the experimental observations of Liang and Mackley. The continuous curves are (a) for A40, $L_1 = 77$ and $P = 5$; (b) for A60, $L_1 = 24$ and $P = 3$; (c) for A80 $L_1 = 4.5$ and $P = 1$; and (d) for A100, $L_1 = 0.84$ and $P = 1$. The dashed curves are the asymptotic result $2a_0(Pa_0G(t)/\chi)^{1/3}$.

Table 2
Parameters and results for the different fluids

	S1	A20	A40	A60	A80	A100
Breakup time t_b (in s)	16	0.34	0.7	1.2	1.8	2.8
Finite extension limit L_1	20	77	77	24	4.5	0.84
L_1 from Eq. (18) with Eq. (17)	47	38	89	15	6.5	3.2
Capillary pressure $\chi/(a_0 \Sigma g_i)$	0.14	45	3.19	0.76	0.36	0.15
Pre-stretch P	1	45	5	3	1	1

Hence the effective single relaxation rate of the fluids in the LFR, as measured by Liang and Mackley from the best straight line fitted through the logarithm of the diameter plotted as a function of time until just before breakup, is set by the finite extension limit. This deduction is clearly a result of our analysis which is based on a particular constitutive equation, that for uncoupled FENE dumbbells. One can debate whether these equations are sensible. In their defence we point out that they do fit all the experimental observations reasonably well, and that they do provide an explanation of how fluids can appear identical in simple shear but significantly different in extension. Of course the values of the finite extension limit found from the LFR for the different fluids range from very plausible for S1 and A20–A60, through questionable for A80, to absurd for A100. But this difficulty of placing a molecular interpretation on the finite extension limit has occurred in the analysis of other experiments. Hence, more thought is needed about the form of the constitutive equation.

Acknowledgements

This collaborative study was made possible by a Royal Society Kapitza Fellowship for V.M. Entov at DMPTP, University of Cambridge (1994), by Grant N M69000 from International Science Foundation, and by Grant ‘Strong flows of polymer solutions’ – INTAS – 93-0279 which are gratefully acknowledged. M. Mackley provided the data of experiments performed at his laboratory and discussions with him were invaluable for this research. The work was finalised in the framework of Programme ‘Dynamics of Complex fluids’ at the Isaac Newton Institute for Mathematical Sciences, Cambridge, 1996.

References

[1] A.V. Bazilevsky, V.M. Entov, A.N. Rozhkov, Liquid filament microrheometer and some of its applications, in D.R. Oliver (Ed.), Proc. 3rd European Rheology Conference, Elsevier, London and New York, 1990, pp. 41–43.
[2] R.F. Liang, M.R. Mackley, Rheological characterisation of the time and strain dependence of polyisobutylene solutions, J. Non-Newtonian Fluid Mech. 52 (1994) 387.